Anisotropic Exciton Transport in a Lamellar $CsPbBr_3$ Nanocrystal Superlattice

*Thomas J. Sheehan[1], Taras V. Sekh[2,3], Maryna I. Bodnarchuk[2,3], Maksym V. Kovalenko[2,3], and William A. Tisdale[1]**

Author Addresses:

[1]Department of Chemical Engineering, Massachusetts Institute of Technology, Cambridge, Massachusetts 02139, United States

[2]Institute of Inorganic Chemistry, Department of Chemistry and Applied Biosciences, ETH Zürich, 8093 Zürich, Switzerland

[3]Laboratory for Thin Films and Photovoltaics, Empa−Swiss Federal Laboratories for Materials Science and Technology, 8600 Dübendorf, Switzerland

Keywords: Nanocrystals, Lead Halide Perovskites, Superlattices, Energy Transfer, Exciton Diffusion, Anisotropic Transport, Microscopy

ABSTRACT

Colloidal self-assembly is one strategy for engineering anisotropic properties into otherwise isotropic materials. In this work, we demonstrate anisotropic exciton transport in an A_2B-type superlattice containing columns of 5.3 nm $CsPbBr_3$ nanocubes assembled into a hexagonal lattice around 6.5 nm LaF_3 nanodisks. Using transient photoluminescence microscopy, we determined that diffusivity along the fast axis of the superlattice is more than twice as large as the slow axis at $T = 5$ K, but that anisotropy is greatly suppressed at room temperature. Calculations of the diffusivity anisotropy ratio based on Förster theory overestimate the measured values, highlighting the limitations of this theory in completely describing exciton transport. Overall, our results demonstrate how self-assembly of colloidal nanocrystals can be used to engineer directional energy transport, and raise more questions about the microscopic nature of dipole coupling in $CsPbBr_3$ NC superlattices.

The self-assembly of semiconducting nanocrystals (NCs) into mesoscopic assemblies provides opportunities to tune the properties of NC solids beyond adjusting the size and composition of the constituent NCs. The optoelectronic behavior of NC assemblies can be altered significantly by inter-particle interactions, which in turn are modulated by structural factors such as the relative position and orientation of NCs within the material.[1–5] Furthermore, synthetic advancements have enabled the self-assembly of different types of NCs into highly ordered superlattices with a wide variety of tightly controlled structures.[6]

Within the vast design space of NC superlattices, superlattices containing $CsPbBr_3$ perovskite NCs have gained particular attention for structural diversity and their potential to exhibit collective behaviors such as superfluorescence, a form of coherent light emission enabled by strong interactions between NCs.[2,7–10] The cubic shape of $CsPbBr_3$ NCs can also cause them to assemble into different superlattice structures than those containing spherical NCs, including lamellar structures containing columns of $CsPbBr_3$ NCs separated by nanodisks.[8,11] Due to the differences in interparticle separation, the interactions between $CsPbBr_3$ NCs are expected to be stronger along the direction of the columns than between columns. These lamellar structures therefore have the potential to introduce strong directional dependence to the optoelectronic behavior of these materials beyond that seen within individual NCs or in other superlattice structures.

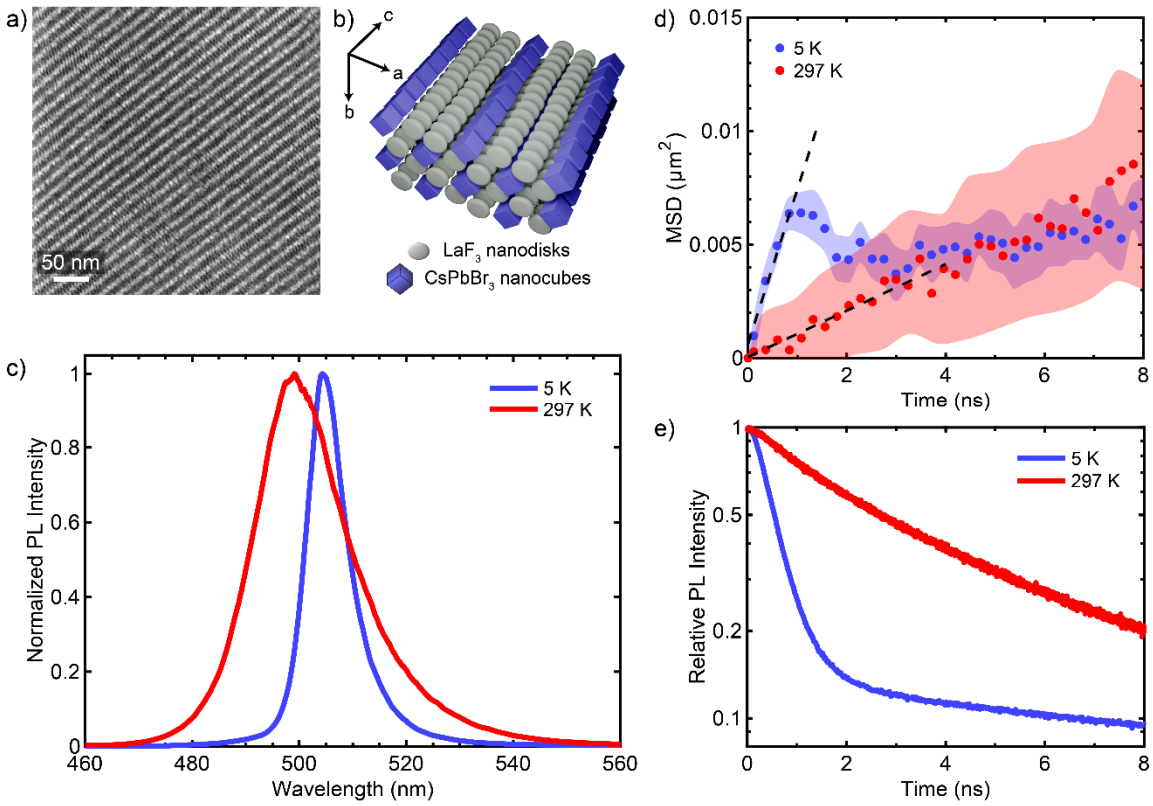

Figure 1. a) DF-STEM image of the lamellar A_2B-type superlattice, showing alternating columns of $CsPbBr_3$ nanocubes and LaF_3 nanodisks aligned parallel to the substrate. b) Structural model of lamellar A_2B-type superlattice, showing the $CsPbBr_3$ NC columns oriented along the *c*-axis and the hexagonal pattern of columns in the *ab*-plane. c) Photoluminescence spectrum of the $CsPbBr_3$ NCs in the A_2B-type superlattice at T = 5 K and room temperature (T = 297 K). d) Mean squared displacement (MSD) of the exciton population along one dimension at 5 K and 297 K. The shaded regions indicate the standard deviation of the MSDs measured in each 240 ps interval at 5 K and 600 ps interval at 297 K. e) Transient photoluminescence (PL) decay at 5 K and 297 K.

In this paper, we investigate how the anisotropic structure of one such lamellar superlattice with an A_2B-type structure drives anisotropic energy transport within its $CsPbBr_3$ NCs. The A_2B-type structure contains columns of 5.3 nm $CsPbBr_3$ nanocubes oriented parallel to the *c*-axis and arranged in a hexagonal pattern in the *ab*-plane, with each column of $CsPbBr_3$ NCs surrounded by six rows of 6.5 nm LaF_3 nanodisks (Figure 1a, 1b). The LaF_3 nanodisks serve as dielectric spacers, which guide the structure of the lattice but generally do not otherwise impact its optoelectronic behavior.[8] The excitonic and photoluminescence behavior of this superlattice is determined by the $CsPbBr_3$ NCs and their interactions (Figure 1c). Using time-resolved photoluminescence

microscopy, we measure the directionality of exciton transport in this superlattice. We show that exciton transport in this structure varies dramatically depending on the direction of transport, with the exciton diffusivity under some conditions varying by a factor of 2-3 depending on the direction. By comparing our measurements of excitonic behavior in the A_2B-type superlattice to the quantitative predictions of Förster theory, we show that although Förster theory does not completely describe exciton transport in this system, the anisotropic exciton transport can be attributed to the stronger dipole couplings among $CsPbBr_3$ NCs within a single column of the superlattice than between separate columns.

The A_2B-type superlattice was fabricated from 5.3 nm $CsPbBr_3$ NCs and 6.5 nm LaF_3 nanodisks, which served as the superlattice building blocks (section S1).[8] Briefly, 5.3 nm $CsPbBr_3$ NCs were synthesized *via* the hot-injection method,[10] followed by ligand-exchange of the pristine, labile oleic acid (OLA) and oleyl amine (OLAm) ligands with didodecyldimethylammonium bromide (DDAB) – a short-chain ligand previously demonstrated to yield colloidally stable and self-assembly-prone NCs.[9,12,13] 6.5 nm LaF_3 nanodisks were synthesized through thermal decomposition of lanthanum trifluoroacetate in a solution of OLA and 1-octadecene.[8,14] The A_2B-type superlattices were then assembled from a mixture of both colloidal components by means of a facile drying-mediated approach over a tilted silicon nitride (SiN_x) membrane.[8,15] Electron microscopy (EM) imaging confirmed the formation of the lamellar A_2B-type superlattice structure, characterized by columns of $CsPbBr_3$ NCs lying flat on the substrate, surrounded by rows of stacked face-to-face nanodisks (Figure 1a, S1a-b). The fabricated superlattices exhibited high substrate coverage of 70% and distinct, highly ordered domains extending laterally over *ca.* 10 μm and with thicknesses of around 5-10 layers of NCs (Figure S1c-d).

To measure exciton transport in these superlattices, we used time-resolved photoluminescence (TRPL) microscopy (section S1.5, Figure S2).[1,16–19] The superlattice was excited using a 405 nm laser pulse focused into a near-diffraction-limited spot on the sample surface, and the resulting PL was refocused and collected using an avalanche photodiode scanning across the image. The intensity profile of the PL at each point in time after the laser excitation was normalized and fit to a convolution of a Gaussian function and the measured profile at $t = 0$.[20] The change in the variances of the Gaussian portions of the convolutions correspond to the mean squared displacement (MSD) of the exciton profile, and the exciton diffusivity can be calculated from the change in the MSD using the equation $D = \frac{\Delta MSD}{2\,\Delta t}$ (see section S2 for further details on the analysis procedure).

To obtain a baseline measurement of the exciton diffusivity, we performed a one-dimensional scan with the photodetector to measure the exciton diffusivity along a single direction in the A_2B-type lamellar superlattice at T = 5 K and at room temperature (T = 297 K). At room temperature, the PL signal decayed steadily with a $1/e$ lifetime of 4.23 ns, and the MSD increased linearly over the first 8 ns, giving an exciton diffusivity of 0.0051±0.0006 cm^2/s (Figure 1d, 1e). However, at 5 K, the decay rate of the PL signal within the first 1 ns after excitation was much faster, having a $1/e$ lifetime of 0.74 ns. The exciton diffusivity in this early time frame was 0.034±0.003 cm^2/s, significantly higher than the diffusivity at room temperature. After about 1 ns, both the PL intensity decay and MSD growth at 5 K slowed dramatically (Figure 1d, 1e). We attribute these changes to trapping and detrapping processes, which would slow down the PL decay rate and can cause non-monotonic behavior in the MSD curve as the excitons transition to a slower diffusivity regime.[21–23] To exclude the impact of trap states, we focus our analysis at 5 K on the early-time evolution of the MSD within 1 ns of laser excitation.

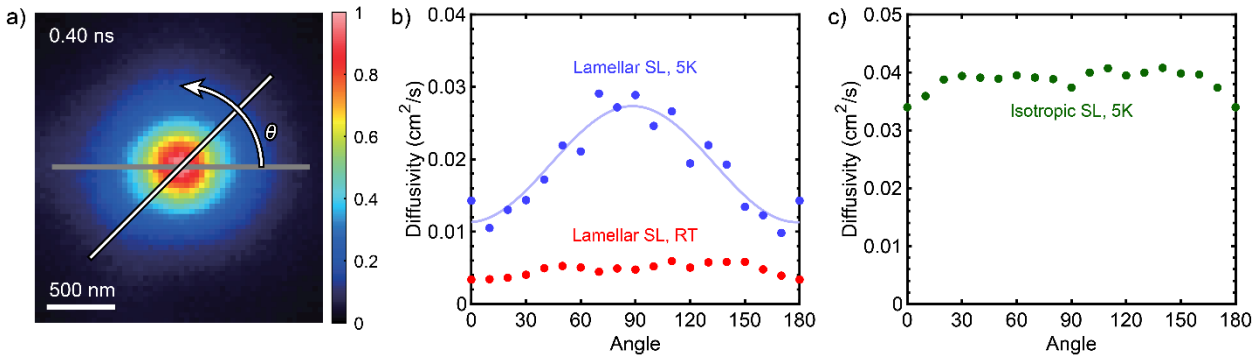

Figure 2. a) Normalized photoluminescence (PL) intensity map for the A_2B-type superlattice 400 ps after laser excitation. Exciton diffusion as a function of angle θ was measured by analyzing the 1D profile at each polar angle. b) Extracted exciton diffusivity as a function of angle in the A_2B-type superlattice at T = 5 K and room temperature (RT, T = 297 K). c) Exciton diffusivity as a function of angle in the isotropic ABO_6-type superlattice, for comparison.

To measure the extent of anisotropy present in the exciton transport in the A_2B-type superlattice, we performed a two-dimensional raster scan with the photodetector to collect the entire time-resolved image of fluorescence from the sample. Then, to measure the exciton diffusivity along a certain angle θ, we extracted a one-dimensional dataset from the 2D image by analyzing the PL along a line passing through the center of the excitation spot and rotated by θ (Fig. 2a). We performed two-dimensional scans of the A_2B-type superlattice at both room temperature and 5 K and extracted the diffusivity along lines oriented at angles from $\theta = 0°$ to 180° in ten-degree increments (Fig. 2b). The diffusivities from 180° to 360° match the values from 0° to 180° due to symmetry. Due to the small diffusion length relative to the spatial extent of the exciton population, the diffusivity as a function of angle at 5 K could be well-fit by a sine wave (section S2.2). When analyzed according to this 2D method, the maximum diffusivity at T = 5 K was found to be 0.027±0.003 cm^2/s at $\theta = 88°$, and the minimum diffusivity was 0.011±0.003 cm^2/s at θ = 178°. The diffusivity anisotropy ratio, defined as the ratio between the maximum and the minimum diffusivity as a function of polar angle, was 2.4. Additionally, the MSD growth along the directions corresponding to both the maximum and minimum exciton diffusivity reached a local maximum after about 1 ns before transitioning to a slower transport regime dominated by

trap states (Figure S3), similar to the MSD growth of the one-dimensional scan at 5 K (Figure 1d). Based on the stronger interactions between neighboring $CsPbBr_3$ NCs within a column relative to $CsPbBr_3$ NCs in different columns, we attribute the maximum diffusivity to transport along the *c*-axis and the minimum diffusivity to transport along a direction in the *ab*-plane. At room temperature, the exciton diffusivities were found to be significantly lower than at 5 K, and the extracted values varied less as a function of polar angle and were no longer well-fit by a sine wave. The maximum measured diffusivity was 0.0059±0.0010 cm^2/s along $\theta = 110°$, and the minimum measured diffusivity was 0.0034±0.0007 cm^2/s along $\theta = 0°$, corresponding to a diffusivity anisotropy ratio of 1.8 at room temperature. We note that taking the direct ratio of the highest and lowest measured diffusivities tends to result in larger predictions of anisotropy since the maximum and minimum values tend to be more affected by noise.

As a control experiment, we performed the same 2D angle-dependent analysis on a different binary $CsPbBr_3$ superlattice containing 17.6 nm and 5.3 nm $CsPbBr_3$ NCs in a cubic ABO_6-type structure.[9] Similarly to the A_2B-type superlattice, these assemblies were formed with comparable quality *via* solvent evaporation on a tilted SiN_x membrane (section S1.2, Figure S4). Based on the symmetry of the assembly structure, exciton transport in this superlattice is expected to be isotropic. We measured the spatiotemporal evolution of photoluminescence in this sample at 5 K and repeated our analysis procedure to extract the exciton diffusivity as a function of angle (Fig. 2c). The average exciton diffusivity in the ABO_6-type superlattice was 0.039 cm^2/s, which is similar to the maximum exciton diffusivity in the A_2B-type superlattice under the same conditions. However, unlike the A_2B-type superlattice, the exciton diffusivity in the ABO_6-type superlattice varied little as a function of angle, with only slight variations due to the noise inherent to the experiment.

Exciton transport in perovskite NC assemblies is typically thought to occur through a series of incoherent hops among perovskite NCs. Due to the insulating ligand shell separating NCs, these hops primarily occur *via* Förster resonance energy transfer (FRET), a mechanism whereby excitons undergo non-radiative energy transfer mediated by transition dipole interactions between NCs.[24–27] Approximating the excitons in NCs as point dipoles in a homogeneous dielectric environment, the FRET rate k_{FRET} between an excited donor NC and an acceptor NC can be expressed in terms of the optical properties of the individual NCs as:

$$k_{FRET} = \frac{k_{rad}}{d^6} \frac{9\kappa^2}{128\,\pi^5 n^4} J \tag{1}$$

Here, k_{rad} is the radiative rate of the donor, d is the distance between the centers of the donor and the acceptor, κ^2 is a factor that ranges from 0 to 4 depending on the orientation of the dipoles, n is the refractive index of the surrounding medium, and J is the spectral overlap integral between the donor and acceptor NCs. This integral term can be expressed as:

$$\int \lambda^4 F_D(\lambda) \sigma_A(\lambda) d\lambda \tag{2}$$

where $F_D(\lambda)$ is the normalized emission spectrum of the donor NC, and $\sigma_A(\lambda)$ is the absorption cross section of the acceptor NC.[28]

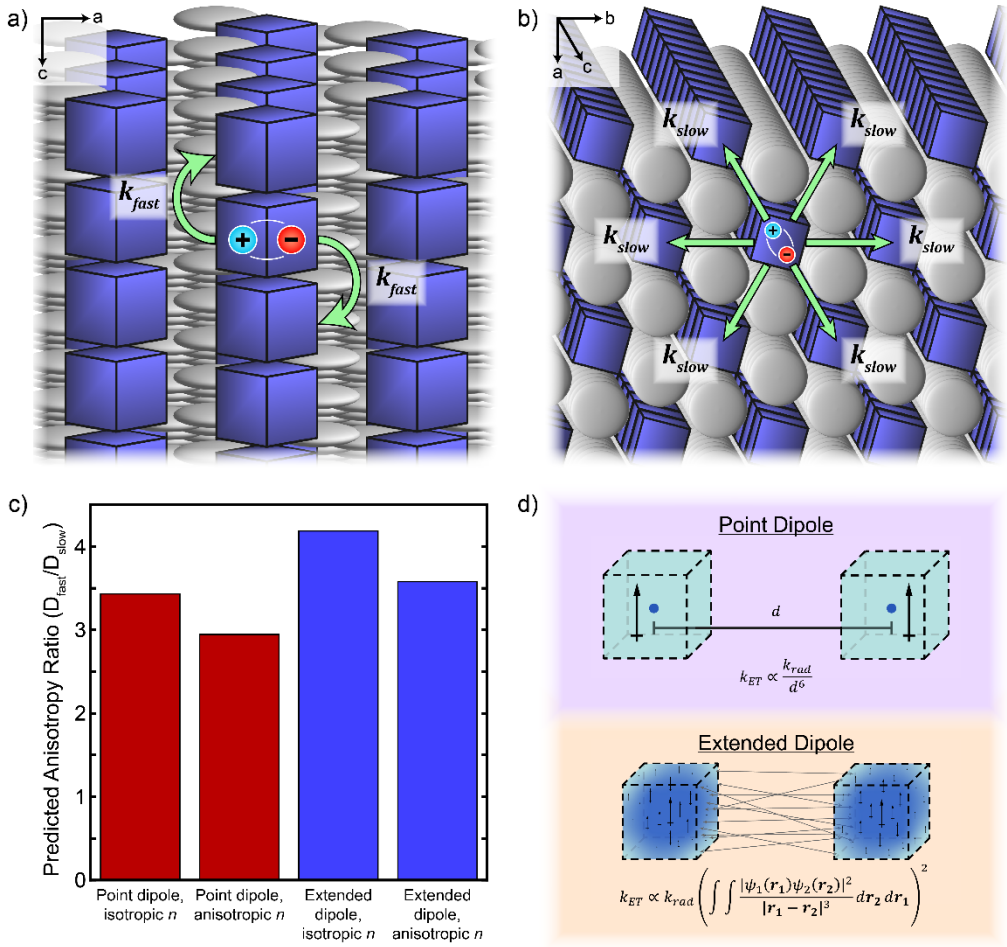

Figure 3. a) Schematic showing the rapid exciton transfer at a rate of k_{fast} in the *c*-axis along the columns of the A_2B-type superlattice. b) Schematic showing the relatively slow exciton transfer at a rate of k_{slow} between different columns of the superlattice in the *ab*-plane. c) Predicted diffusivity anisotropy ratio calculated from FRET theory under different assumptions. d) Schematic showing how dipole-dipole coupling between delocalized excitons differs from point excitons.

The center-to-center distance between adjacent NCs in the same column of the A_2B-type superlattice (~6.4 nm) is about half of the distance between NCs in different columns (~13 nm,). Given the strong $1/d^6$ dependence of the FRET rate on the distance between the donor and the acceptor, the exciton hopping rates between neighboring perovskite NCs in a single column are predicted to be approximately $2^6 = 64$ larger than the exciton hopping rates between perovskite NCs in different columns. This would predict a significantly higher exciton hopping rate along the *c*-axis (k_{fast}, Figure 3a) than in the *ab*-plane (k_{slow}, Figure 3b). However, due to the mechanics

of hopping transport and the structure of the superlattice, the difference between the diffusivities D_{fast} and D_{slow} is significantly smaller than the difference between the exciton hopping rates k_{fast} and k_{slow} in the same directions. Since hops between neighboring columns of $CsPbBr_3$ NCs generally travel a farther distance than hops within a column, each individual hop within a column tends to contribute less to the exciton diffusivity than hops between columns. The hexagonal symmetry of the NC columns (increasing the number of nearest-neighbors within the hexagonal plane) and the contributions of acceptor NCs beyond the nearest-neighbors additionally increase D_{slow} relative to D_{fast}.

To quantitatively analyze our results in the context of FRET theory, we explicitly calculated the expected diffusivity anisotropy ratio by comparing energy transport rates between different pairs of $CsPbBr_3$ NCs in a full 3D model of the A_2B-type superlattice under differing assumptions (section S3.1). Since the spectral properties and the radiative lifetimes of the $CsPbBr_3$ NCs are generally consistent over the length scales of the diffusion imaging experiment, the radiative rate k_{rad} and spectral overlap term J in the FRET rate equation should contribute the same factor to diffusion in all directions and therefore do not contribute to the diffusivity anisotropy. Additionally, given that the PL characteristics of the A_2B-type superlattice are largely independent of polarization at 5 K (figure S6), we approximate the exciton transition dipole orientations as being evenly distributed among the orthogonally oriented bright triplet states such that the κ^2 term equally affects transition rates in different directions.[29] Under these assumptions, the pairwise energy transfer rate depends only on the distance between the NCs d and the refractive index n. If we furthermore assume that the refractive index n is isotropic, such that the transition rates between each pair of QDs are only a function of distance, the expected diffusivity anisotropy ratio is 3.43, which is higher than the observed diffusivity anisotropy ratios of 2.4 and 1.8 at 5 K

and room temperature, respectively (Fig. 3c). However, in reality, the A_2B-type superlattice should have two different refractive indices along the directions parallel and perpendicular to the columns of $CsPbBr_3$ NCs due to the differences in the dielectric properties among the two types of NCs and the organic ligands.[30,31] Using effective medium theory, we estimate that the refractive index in the direction parallel to the columns is 1.79, and the refractive index perpendicular to the columns is 1.70 (section S3.2).[32,33] Accounting for the higher refractive index in the direction of D_{fast} decreases the theoretical diffusivity anisotropy ratio to 2.95, closer to the experimentally observed values (Fig. 3c).

Although these FRET calculations can approximately predict the diffusivity anisotropy ratio in the A_2B-type superlattice at $T = 5$ K, they generally overestimate the observed values, and they do not explain why the value of D_{fast}/D_{slow} is much smaller at room temperature than at 5 K. Additionally, conventional FRET theory within the point dipole approximation is known to dramatically underestimate energy transport rates in NC assemblies by up to several orders of magnitude – especially in assemblies containing $CsPbBr_3$ NCs.[28,34,35] This has often been attributed in part to a failure of the point dipole approximation, which is a questionable approximation when the diameter of NCs is larger than their surface-to-surface separation – especially at cryogenic temperature, when the coherence size of the exciton can extend over the entire NC volume.[36,37] To account for these effects, we used an approach similar to that used by Kodaimati *et al.*,[38] wherein the spatially-extended transition dipoles of the donor and acceptor NCs are approximated as a collection of infinitesimal point dipoles whose strength varies based on the probability distributions of the donor and acceptor wavefunctions, approximated here by the ground state particle-in-a-cube equation. Then, we performed an integration over both wavefunctions to combine the contributions of each pair of point dipoles to the overall transition rate (Fig. 3d, section

S3.3). Based on this method, we obtained predicted diffusivity anisotropy ratios of 4.19 and 3.58, respectively, in the cases of isotropic and anisotropic refractive indices. These values are about 20% higher than the corresponding diffusivity anisotropy ratios obtained using the point dipole approximation with isotropic and anisotropic refractive indices. While these values overestimate the experimental values for the diffusivity anisotropy ratio in the A_2B superlattice at 5 K by an even greater extent than the point-dipole approximation, they do qualitatively capture the trend of increasing exciton transport anisotropy with increasing spatial extent of the exciton at lower sample temperature. However, even assuming the phonon-driven exciton wavefunction localization at room temperature is extensive enough that the point dipole approximation applies, the impact of wavefunction delocalization is not enough to quantitatively explain the difference in diffusivity anisotropy ratio between room temperature and 5 K.

The change in the diffusivity anisotropy ratio across temperature could be additionally explained by other structural and photophysical factors. For example, thermal contraction of the organic ligand layers within the superlattice as the sample is cooled from room temperature to 5 K is expected to decrease the distance between NC surfaces and enhance D_{fast} relative to D_{slow} for delocalized excitons.[39] Systematic variations in the dipole orientation, especially as a function of temperature, could also alter exciton transport in different directions. Additionally, FRET is not the only possible mechanism for exciton transport in these materials; transition dipole interactions beyond the near field, which lead to phenomena such as photon emission-reabsorption or "photon recycling", can also contribute to measured exciton transport rates and could possibly reduce exciton transport anisotropy in the A_2B-type superlattice due to its weaker $1/d^2$ distance dependence compared to FRET.[34,40]

In this work, we demonstrated that colloidal NC assembly can be used as a tool to engineer anisotropic energy transport among excitonic NCs of isotropic shape. Using transient photoluminescence microscopy, we showed that the ratio between the diffusivities in the fastest and the slowest directions in an A_2B-type $CsPbBr_3$ superlattice increases from about 1.8 at room temperature to 2.4 at cryogenic temperatures. We furthermore showed that calculations of exciton diffusivity using transport rates derived from different iterations of FRET theory tend to overestimate the experimentally observed diffusivity anisotropy ratio, and that the predictions based on FRET theory are strongly dependent on the materials assumptions made. Overall, by confirming that anisotropic NC assembly structures can lead to significant anisotropy in energy transport rates, these results highlight the novel behaviors and functionalities that can be achieved through NC self-assembly.

ASSOCIATED CONTENT

Supporting Information.

The following files are available free of charge.

Supplementary Information (PDF)

- Detailed materials and methods (synthesis of $CsPbBr_3$ nanocrystals, synthesis of LaF_3 nanocrystals, self-assembly process, EM characterization, spectroscopic characterization), data analysis procedure for extracting exciton diffusivities, calculation of theoretical exciton diffusivity anisotropy factors, structural parameters of A_2B-type superlattice

Corresponding Author

*William A. Tisdale. Email: tisdale@mit.edu

Author Contributions

The manuscript was written through contributions of all authors. All authors have given approval to the final version of the manuscript.

Funding Sources

U.S. Department of Energy, Basic Energy Sciences: DE-SC0019345 (MIT)

Office of Naval Research under Grant No. N629092512073

The Swiss Federal Laboratory for Materials Science and Technology (Empa, Switzerland)

The Swiss National Science Foundation under grant number 200021-231778

ACKNOWLEDGMENT

Time-resolved microscopy and other spectroscopic characterization at MIT were supported by the U.S. Department of Energy, Office of Science, Basic Energy Sciences, under award no. DE-

SC0019345. T.J.S. was partially supported by a Chemical Engineering Mathworks Fellowship. Synthesis and characterization of nanocrystal superlattices at ETH and Empa was supported by the Office of Naval Research under Grant No. N629092512073, the Swiss Federal Laboratory for Materials Science and Technology (Empa, Switzerland), and by the Swiss National Science Foundation (grant number 200021-231778, project CHIP-QD).

ABBREVIATIONS

NC, nanocrystal; EM, electron microscopy; TR, time-resolved; PL, photoluminescence; MSD, mean square displacement; FRET, Förster resonance energy transfer

References:

(1) Akselrod, G. M.; Prins, F.; Poulikakos, L. V.; Lee, E. M. Y.; Weidman, M. C.; Mork, A. J.; Willard, A. P.; Bulović, V.; Tisdale, W. A. Subdiffusive Exciton Transport in Quantum Dot Solids. *Nano Lett.* **2014**, *14* (6), 3556–3562. https://doi.org/10.1021/nl501190s.

(2) Rainò, G.; Becker, M. A.; Bodnarchuk, M. I.; Mahrt, R. F.; Kovalenko, M. V.; Stöferle, T. Superfluorescence from Lead Halide Perovskite Quantum Dot Superlattices. *Nature* **2018**, *563* (7733), 671–675. https://doi.org/10.1038/s41586-018-0683-0.

(3) Zhang, Z.; Sung, J.; Toolan, D. T. W.; Han, S.; Pandya, R.; Weir, M. P.; Xiao, J.; Dowland, S.; Liu, M.; Ryan, A. J.; Jones, R. A. L.; Huang, S.; Rao, A. Ultrafast Exciton Transport at Early Times in Quantum Dot Solids. *Nat. Mater.* **2022**, 1–7. https://doi.org/10.1038/s41563-022-01204-6.

(4) Tang, X.; Rossi, D.; Cheon, J.; Son, D. H. Effects of Electronic Coupling on Bright and Dark Excitons in a 2D Array of Strongly Confined CsPbBr3 Quantum Dots. *Chem. Mater.* **2022**, *34* (16), 7181–7189. https://doi.org/10.1021/acs.chemmater.2c00683.

(5) Blach, D. D.; Lumsargis-Roth, V. A.; Chuang, C.; Clark, D. E.; Deng, S.; Williams, O. F.; Li, C. W.; Cao, J.; Huang, L. Environment-Assisted Quantum Transport of Excitons in Perovskite Nanocrystal Superlattices. *Nat Commun* **2025**, *16* (1), 1270. https://doi.org/10.1038/s41467-024-55812-8.

(6) Shevchenko, E. V.; Talapin, D. V.; Kotov, N. A.; O'Brien, S.; Murray, C. B. Structural Diversity in Binary Nanoparticle Superlattices. *Nature* **2006**, *439* (7072), 55–59. https://doi.org/10.1038/nature04414.

(7) Cherniukh, I.; Raino, G.; Stoferle, T.; Burian, M.; Travesset, A.; Naumenko, D.; Amenitsch, H.; Erni, R.; Mahrt, R. F.; Bodnarchuk, M. I.; Kovalenko, M. V. Perovskite-Type Superlattices from Lead Halide Perovskite Nanocubes. *Nature* **2021**, *593* (7860), 535–542. https://doi.org/10.1038/s41586-021-03492-5.

(8) Cherniukh, I.; Rainò, G.; Sekh, T. V.; Zhu, C.; Shynkarenko, Y.; John, R. A.; Kobiyama, E.; Mahrt, R. F.; Stöferle, T.; Erni, R.; Kovalenko, M. V.; Bodnarchuk, M. I. Shape-Directed

Co-Assembly of Lead Halide Perovskite Nanocubes with Dielectric Nanodisks into Binary Nanocrystal Superlattices. *ACS Nano* **2021**, *15* (10), 16488–16500. https://doi.org/10.1021/acsnano.1c06047.

(9) Sekh, T. V.; Cherniukh, I.; Kobiyama, E.; Sheehan, T. J.; Manoli, A.; Zhu, C.; Athanasiou, M.; Sergides, M.; Ortikova, O.; Rossell, M. D.; Bertolotti, F.; Guagliardi, A.; Masciocchi, N.; Erni, R.; Othonos, A.; Itskos, G.; Tisdale, W. A.; Stöferle, T.; Rainò, G.; Bodnarchuk, M. I.; Kovalenko, M. V. All-Perovskite Multicomponent Nanocrystal Superlattices. *ACS Nano* **2024**, *18* (11), 8423–8436. https://doi.org/10.1021/acsnano.3c13062.

(10) Protesescu, L.; Yakunin, S.; Bodnarchuk, M. I.; Krieg, F.; Caputo, R.; Hendon, C. H.; Yang, R. X.; Walsh, A.; Kovalenko, M. V. Nanocrystals of Cesium Lead Halide Perovskites (CsPbX(3), X = Cl, Br, and I): Novel Optoelectronic Materials Showing Bright Emission with Wide Color Gamut. *Nano Lett* **2015**, *15* (6), 3692–3696. https://doi.org/10.1021/nl5048779.

(11) Cherniukh, I.; Sekh, T. V.; Rainò, G.; Ashton, O. J.; Burian, M.; Travesset, A.; Athanasiou, M.; Manoli, A.; John, R. A.; Svyrydenko, M.; Morad, V.; Shynkarenko, Y.; Montanarella, F.; Naumenko, D.; Amenitsch, H.; Itskos, G.; Mahrt, R. F.; Stöferle, T.; Erni, R.; Kovalenko, M. V.; Bodnarchuk, M. I. Structural Diversity in Multicomponent Nanocrystal Superlattices Comprising Lead Halide Perovskite Nanocubes. *ACS Nano* **2022**, *16* (5), 7210–7232. https://doi.org/10.1021/acsnano.1c10702.

(12) Dong, Y.; Qiao, T.; Kim, D.; Parobek, D.; Rossi, D.; Son, D. H. Precise Control of Quantum Confinement in Cesium Lead Halide Perovskite Quantum Dots via Thermodynamic Equilibrium. *Nano Lett.* **2018**, *18* (6), 3716–3722. https://doi.org/10.1021/acs.nanolett.8b00861.

(13) Boehme, S. C.; Bodnarchuk, M. I.; Burian, M.; Bertolotti, F.; Cherniukh, I.; Bernasconi, C.; Zhu, C.; Erni, R.; Amenitsch, H.; Naumenko, D.; Andrusiv, H.; Semkiv, N.; John, R. A.; Baldwin, A.; Galkowski, K.; Masciocchi, N.; Stranks, S. D.; Rainò, G.; Guagliardi, A.; Kovalenko, M. V. Strongly Confined CsPbBr3 Quantum Dots as Quantum Emitters and Building Blocks for Rhombic Superlattices. *ACS Nano* **2023**, *17* (3), 2089–2100. https://doi.org/10.1021/acsnano.2c07677.

(14) Paik, T.; Diroll, B. T.; Kagan, C. R.; Murray, C. B. Binary and Ternary Superlattices Self-Assembled from Colloidal Nanodisks and Nanorods. *J. Am. Chem. Soc.* **2015**, *137* (20), 6662–6669. https://doi.org/10.1021/jacs.5b03234.

(15) Bodnarchuk, M. I.; Kovalenko, M. V.; Heiss, W.; Talapin, D. V. Energetic and Entropic Contributions to Self-Assembly of Binary Nanocrystal Superlattices: Temperature as the Structure-Directing Factor. *J. Am. Chem. Soc.* **2010**, *132* (34), 11967–11977. https://doi.org/10.1021/ja103083q.

(16) Akselrod, G. M.; Deotare, P. B.; Thompson, N. J.; Lee, J.; Tisdale, W. A.; Baldo, M. A.; Menon, V. M.; Bulovic, V. Visualization of Exciton Transport in Ordered and Disordered Molecular Solids. *Nat Commun* **2014**, *5*, 3646. https://doi.org/10.1038/ncomms4646.

(17) Ginsberg, N. S.; Tisdale, W. A. Spatially Resolved Exciton and Charge Transport in Emerging Semiconductors. *Annu Rev Phys Chem* **2019**. https://doi.org/10.1146/annurev-physchem-052516-050703.

(18) Nagaya Wong, N.; Ha, S. K.; Williams, K.; Shcherbakov-Wu, W.; Swan, J. W.; Tisdale, W. A. Robust Estimation of Charge Carrier Diffusivity Using Transient Photoluminescence Microscopy. *J. Chem. Phys.* **2022**, *157* (10), 104201. https://doi.org/10.1063/5.0100075.

(19) Vazquez, G. D. B.; Morganti, G. L. G.; Block, A.; van Hulst, N. F.; Liebel, M.; Tielrooij, K.-J. Spatiotemporal Microscopy: Shining Light on Transport Phenomena. *Advanced Electronic Materials* **2024**, *10* (2), 2300584. https://doi.org/10.1002/aelm.202300584.
(20) Hickey, C. L.; Grumstrup, E. M. Reduced Artifact Approach for Determining Diffusion Coefficients in Time-Resolved Microscopy. *J. Phys. Chem. C* **2020**, *124* (25), 14016–14021. https://doi.org/10.1021/acs.jpcc.0c02302.
(21) Ziegler, J. D.; Zipfel, J.; Meisinger, B.; Menahem, M.; Zhu, X.; Taniguchi, T.; Watanabe, K.; Yaffe, O.; Egger, D. A.; Chernikov, A. Fast and Anomalous Exciton Diffusion in Two-Dimensional Hybrid Perovskites. *Nano Lett.* **2020**, *20* (9), 6674–6681. https://doi.org/10.1021/acs.nanolett.0c02472.
(22) Adejumobi, O. P.; Mantsevich, V. N.; Palyulin, V. V. Diffusion of Fast and Slow Excitons with an Exchange in Quasi-Two-Dimensional Systems. *Phys. Rev. E* **2024**, *110* (5), 054139. https://doi.org/10.1103/PhysRevE.110.054139.
(23) Tan, R.; Xu, X.; Liu, M.; Qu, J.; Shi, H.; Li, W.; Yang, J.; Gao, B.; Li, X. Three-Stage Diffusion Process of Carriers in Thin InSe. *Advanced Optical Materials* **2025**, *13* (14), 2403449. https://doi.org/10.1002/adom.202403449.
(24) Penzo, E.; Loiudice, A.; Barnard, E. S.; Borys, N. J.; Jurow, M. J.; Lorenzon, M.; Rajzbaum, I.; Wong, E. K.; Liu, Y.; Schwartzberg, A. M.; Cabrini, S.; Whitelam, S.; Buonsanti, R.; Weber-Bargioni, A. Long-Range Exciton Diffusion in Two-Dimensional Assemblies of Cesium Lead Bromide Perovskite Nanocrystals. *ACS Nano* **2020**, *14* (6), 6999–7007. https://doi.org/10.1021/acsnano.0c01536.
(25) Lichtenegger, M. F.; Drewniok, J.; Bornschlegl, A.; Lampe, C.; Singldinger, A.; Henke, N. A.; Urban, A. S. Electron–Hole Binding Governs Carrier Transport in Halide Perovskite Nanocrystal Thin Films. *ACS Nano* **2022**, *16* (4), 6317–6324. https://doi.org/10.1021/acsnano.2c00369.
(26) Bornschlegl, A. J.; Lichtenegger, M. F.; Luber, L.; Lampe, C.; Bodnarchuk, M. I.; Kovalenko, M. V.; Urban, A. S. Dark-Bright Exciton Splitting Dominates Low-Temperature Diffusion in Halide Perovskite Nanocrystal Assemblies. *Advanced Energy Materials* **2024**, *n/a* (n/a), 2303312. https://doi.org/10.1002/aenm.202303312.
(27) Sheehan, T. J.; Saris, S.; Tisdale, W. A. Exciton Transport in Perovskite Materials. *Advanced Materials* **2025**, *37* (25), 2415757. https://doi.org/10.1002/adma.202415757.
(28) Mork, A. J.; Weidman, M. C.; Prins, F.; Tisdale, W. A. Magnitude of the Förster Radius in Colloidal Quantum Dot Solids. *J. Phys. Chem. C* **2014**, *118* (25), 13920–13928. https://doi.org/10.1021/jp502123n.
(29) Tamarat, P.; Prin, E.; Berezovska, Y.; Moskalenko, A.; Nguyen, T. P. T.; Xia, C.; Hou, L.; Trebbia, J.-B.; Zacharias, M.; Pedesseau, L.; Katan, C.; Bodnarchuk, M. I.; Kovalenko, M. V.; Even, J.; Lounis, B. Universal Scaling Laws for Charge-Carrier Interactions with Quantum Confinement in Lead-Halide Perovskites. *Nat Commun* **2023**, *14* (1), 229. https://doi.org/10.1038/s41467-023-35842-4.
(30) Yang, Z.; Surrente, A.; Galkowski, K.; Miyata, A.; Portugall, O.; Sutton, R. J.; Haghighirad, A. A.; Snaith, H. J.; Maude, D. K.; Plochocka, P.; Nicholas, R. J. Impact of the Halide Cage on the Electronic Properties of Fully Inorganic Cesium Lead Halide Perovskites. *ACS Energy Lett.* **2017**, *2* (7), 1621–1627. https://doi.org/10.1021/acsenergylett.7b00416.
(31) Polyanskiy, M. N. Refractiveindex.Info Database of Optical Constants. *Sci Data* **2024**, *11* (1), 94. https://doi.org/10.1038/s41597-023-02898-2.

(32) Reyes, E.; Krokhin, A. A.; Roberts, J. Effective Dielectric Constants of Photonic Crystal of Aligned Anisotropic Cylinders and the Optical Response of a Periodic Array of Carbon Nanotubes. *Phys. Rev. B* **2005**, *72* (15), 155118. https://doi.org/10.1103/PhysRevB.72.155118.
(33) Godin, Y. A. Effective Properties of Periodic Tubular Structures. *The Quarterly Journal of Mechanics and Applied Mathematics* **2016**, *69* (2), 181–193. https://doi.org/10.1093/qjmam/hbw003.
(34) Yuan, R.; Roberts, T. D.; Brinn, R. M.; Choi, A. A.; Park, H. H.; Yan, C.; Ondry, J. C.; Khorasani, S.; Masiello, D. J.; Xu, K.; Alivisatos, A. P.; Ginsberg, N. S. A Composite Electrodynamic Mechanism to Reconcile Spatiotemporally Resolved Exciton Transport in Quantum Dot Superlattices. *Science Advances* **2023**, *9* (42), eadh2410. https://doi.org/10.1126/sciadv.adh2410.
(35) Shcherbakov-Wu, W.; Saris, S.; Sheehan, T. J.; Wong, N. N.; Powers, E. R.; Krieg, F.; Kovalenko, M. V.; Willard, A. P.; Tisdale, W. A. Persistent Enhancement of Exciton Diffusivity in CsPbBr3 Nanocrystal Solids. *Science Advances* **2024**, *10* (8), eadj2630. https://doi.org/10.1126/sciadv.adj2630.
(36) Zhu, C.; Boehme, S. C.; Feld, L. G.; Moskalenko, A.; Dirin, D. N.; Mahrt, R. F.; Stöferle, T.; Bodnarchuk, M. I.; Efros, A. L.; Sercel, P. C.; Kovalenko, M. V.; Rainò, G. Single-Photon Superradiance in Individual Caesium Lead Halide Quantum Dots. *Nature* **2024**, *626* (7999), 535–541. https://doi.org/10.1038/s41586-023-07001-8.
(37) Feld, L. G.; Boehme, S. C.; Sabisch, S.; Frenkel, N.; Yazdani, N.; Morad, V.; Zhu, C.; Kim, T.; Canossa, S.; Svyrydenko, M.; Tao, R.; Bodnarchuk, M. I.; Lubin, G.; Kazes, M.; Wood, V.; Oron, D.; Rainò, G.; Kovalenko, M. V. Phonon-Driven Wavefunction Localization Enhances Room-Temperature Single-Photon Purity in Large Hybrid Lead Halide Perovskite Quantum Dots. *Nat Commun* **2026**. https://doi.org/10.1038/s41467-026-68607-w.
(38) Kodaimati, M. S.; Wang, C.; Chapman, C.; Schatz, G. C.; Weiss, E. A. Distance-Dependence of Interparticle Energy Transfer in the Near-Infrared within Electrostatic Assemblies of PbS Quantum Dots. *ACS Nano* **2017**, *11* (5), 5041–5050. https://doi.org/10.1021/acsnano.7b01778.
(39) Filippi, U.; Toso, S.; Zaffalon, M. L.; Pianetti, A.; Li, Z.; Marras, S.; Goldoni, L.; Meinardi, F.; Brovelli, S.; Baranov, D.; Manna, L. Cooling-Induced Order–Disorder Phase Transition in CsPbBr3 Nanocrystal Superlattices. *Advanced Materials* **2025**, *37* (3), 2410949. https://doi.org/10.1002/adma.202410949.
(40) Luo, Y.; Dang, Z.; Meng, L.; Chen, Z.; Li, Z.; Lu, T.; Rao, X.; Zhao, S.; Sun, Q.; Gao, P. Universal, Predominant Exciton Transfer in Perovskite Nanocrystal Solids. *Sci. China Mater.* **2024**. https://doi.org/10.1007/s40843-023-2854-7.

TOC Graphic:

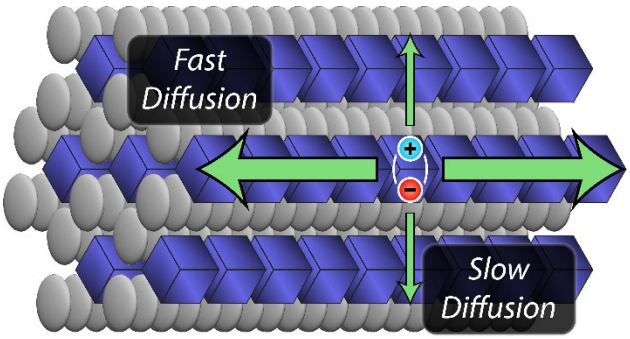

Supplementary Information for:

Anisotropic Exciton Transport in a Lamellar $CsPbBr_3$ Nanocrystal Superlattice

*Thomas J. Sheehan[1], Taras V. Sekh[2,3], Maryna I. Bodnarchuk[2,3], Maksym V. Kovalenko[2,3], and William A. Tisdale[1]**

Author Addresses:

[1]Department of Chemical Engineering, Massachusetts Institute of Technology, Cambridge, Massachusetts 02139, United States

[2]Institute of Inorganic Chemistry, Department of Chemistry and Applied Biosciences, ETH Zürich, 8093 Zürich, Switzerland

[3]Laboratory for Thin Films and Photovoltaics, Empa−Swiss Federal Laboratories for Materials Science and Technology, 8600 Dübendorf, Switzerland

Keywords: Nanocrystals, Lead Halide Perovskites, Superlattices, Energy Transfer, Exciton Diffusion, Anisotropic Transport, Microscopy

S1. Materials and Methods

1.1. Synthesis of $CsPbBr_3$ NCs

Preparation of 0.12M Cs-OA stock solution, adapted from Ref.[1,2]

195.4 mg of Cs_2CO_3 (99.9%, Aldrich), 1 mL oleic acid (OLA, 90%, Aldrich, vacuum-dried at 100 °C), and 9 mL 1-octadecene (ODE, for synthesis, Aldrich, distilled) were loaded in a 25 mL round-bottom flask. The reaction mixture was purged with N_2 for 1 h at 120 °C and 10 min at 150 °C, then cooled to room temperature and stored in the glovebox.

Preparation of 0.15M Cs-OLA stock solution, adapted from Ref.[1,2]

200.0 mg of Cs_2CO_3, 0.6 mL OLA (vacuum-dried at 100 °C), and 7.5 mL ODE (distilled) were loaded in a 25 mL round-bottom flask. The reaction mixture was degassed for 20 min at 100 °C, then purged with N_2 at 120 °C until the Cs_2CO_3 had fully reacted with the OLA. The solution was cooled to room temperature and stored in the glovebox.

Synthesis of 5.3 nm $CsPbBr_3$ NCs, adapted from Ref.[1–4]

75 mg of $PbBr_2$ (99.999%, Aldrich) and 180 mg of $ZnBr_2$ (99.9%, Alfa Aesar) were suspended in 5 mL of mesitylene (99%, Acros Organics, dried) in a 25 mL three-neck flask and degassed five times at room temperature. Then, the suspension was quickly heated under N_2. When the temperature reached 120 °C, 2 mL of OLA (vacuum-dried at 100 °C) and 2 mL of OLAm (min. 95%, Strem, distilled) were injected. Later, when the temperature reached 146 °C, 0.4 mL of the 0.15M Cs-OLA solution, heated to a temperature of 100 °C, was quickly injected. The reaction mixture was then immediately placed in an ice-water bath to cool it to room temperature, then centrifuged at 12100 rpm (20130 rcf) for 3 mins. The precipitate was discarded, and the supernatant was destabilized with 27.5 mL of ethyl acetate (HPLC Plus, 99.9%, Aldrich). The solution was again centrifuged at 12100 rpm (20130 rcf) for 5 min. The supernatant was discarded,

and the precipitate was redispersed in 1.8 mL of toluene (anhydrous, 99.8%, Aldrich). Afterwards, the OLA/OLAm ligands were exchanged for didodecyldimethylammonium bromide (DDAB, 98%, Aldrich) by adding 90 µL of 0.01M DDAB solution in toluene. The solution was stirred for 2h, centrifuged at 12100 rpm (20130 rcf) for 6 min, and the precipitate was discarded.

Synthesis of 17.6 nm $CsPbBr_3$ NCs, adapted from Ref.[1,5]

44.6 mg of PbO (99.999%, Aldrich), 119.4 mg of phenacyl bromide (98%, Aldrich), and 1 mL of OA (vacuum-dried at 100 °C) were suspended in 5 mL of ODE in a 25 mL three-neck flask and heated to 220 °C. 0.6 mL of OLAm (distilled) was injected, causing the solution to become red before slowly turning orange and yellow over the course of ~10 min. The reaction was cooled slightly to 210 °C, and 0.5 mL of the 0.12M Cs-OLA solution, preheated to 100 °C, was quickly injected. The solution was annealed at 210 °C for 1h, then placed in an ice bath to cool down to room temperature. Then, the solution was centrifuged at 3000 rpm (1240 rcf) for 5 min, the dark brown supernatant was discarded, and the precipitate was redispersed in 2 mL of toluene. The solution was centrifuged again at 3000 rpm (1240 rcf) for 3 min, and the precipitate was discarded. Then, the OLA/OLAm ligands on the NCs were exchanged for DDAB. 60 µL of a DDAB/$PbBr_2$ stock solution containing 36.7 mg $PbBr_2$ and 92 mg DDAB dissolved in 3 mL toluene was added to the NC dispersion, and the solution was stirred for 1h. The solution was then destabilized by adding 1.2 mL of ethyl acetate, centrifuged at 12100 rpm (20130 rcf) for 2 min, and redispersed in 0.4 mL of toluene.

1.2. Synthesis of LaF_3 nanodisks

6.5 nm LaF_3 nanodisks were synthesized following procedures adopted from Ref.[6,7] First, lanthanum trifluoroacetate was synthesized by reacting 3.24 g La_2O_3 (Sigma-Aldrich, 99.999%) and 16 mL trifluoroacetic acid (Aldrich, 99%) in 16 mL of water under reflux (93 °C) for 1h.

Unreacted acid and water were removed by evaporation under vacuum at 60 °C, leaving a white product that was dried overnight under a vacuum.

To synthesize LaF_3 nanodisks, 192 mg of lanthanum trifluoroacetate, LiF (31.2 mg, Sigma-Aldrich, 99.99%), 6 mL of OLA (vacuum-dried at 100 °C), and 6 mL of ODE (90%, Aldrich, distilled) were placed in a 25 mL three-neck flask and degassed for 2 h at 125 °C. The solution was placed under N_2 and heated at a rate of 15 °C/min to 295 °C and maintained at this temperature for 32 min. Then, the solution was cooled to room temperature and destabilized using 3 mL of hexane (Aldrich, anhydrous, 95%) with 30 mL ethanol (Merck, 99.8%). The solution was centrifuged at 2200 rcf for 2 min, and the NCs in the precipitate were washed twice with hexane mixed with 10-30 µL OLA and ethanol at a 1:1 volumetric ratio. Then, the NCs were redispersed in 3 mL hexane and centrifuged at 2200 rcf for 2 min to remove residual LiF in the precipitate.

1.3. Preparation of multicomponent NC superlattices

Binary superlattices (SLs) were prepared following the drying-mediated self-assembly method described in Ref.[1,6] SLs were grown on SiN_x membrane substrates (Agar S171-2 for A_2B-type SLs, Norcada NT050A for ABO_6-type SLs). 30-35 µL of a mixture of the constituent NCs in either SL structure was prepared in anhydrous toluene and transferred into a tilted 2 mL vial that also contained the SiN_x substrate. The vial was left tilted in a vacuum chamber (~0.5 atm, room temperature) until the solvent evaporated. For the A_2B-type SLs, the NC mixture contained 8 µL of 5.3 nm $CsPbBr_3$ NCs (1.8 µM), 5 µL of 6.5 nm LaF_3 nanodisks (5 mg/mL), 6 µL of OLA and OLAm mixture (8 mM), and 15 µL of anhydrous toluene. For the ABO_6-type SLs, the NC mixture contained 3 µL of 9.6 µM 5.3 nm $CsPbBr_3$ NCs, 4 µL of 0.9 µM 17.6 nm $CsPbBr_3$ NCs, and 25 µL of anhydrous toluene.

1.4. Electron Microscopy Characterization

TEM, BF-STEM and DF-STEM images were collected on a JEOL JEM 2200FS electron microscope at an accelerating voltage of 200 kV. Image analysis was performed using ImageJ.

1.5. Transient photoluminescence microscopy (TPLM)

An illustration of our spectroscopic setup can be found in Figure S2. Nanocrystal superlattices were mounted on a piezo stage (controlled by an attocube ANC350) in a closed-cycle liquid helium cryostat (Montana Instruments Cryostation s100) and placed under vacuum. For the A_2B-type SLs, the light source was a Ti:sapphire laser (Mira 900) operating at 76 MHz. The Mira was set to output 810 nm ultrafast pulses (~150 fs) that were frequency-doubled to 405 nm. For the ABO_6-type SL, the light source was a 405 nm pulsed laser (PicoQuant LDH-P-C-405M, driven by a PDL 800-D, pulse width < 100 ps). In either case, the laser fluence at the sample surface was set to ~0.012 μJ/cm^2. The excitation light was focused onto a near diffraction-limited spot on the surface of the sample using a microscope objective lens (Zeiss EC Epiplan-Neofluar 100X/0.85 NA). The fluorescence from the sample was collected by the same objective and filtered using a dichroic mirror (Semrock, Di02-R405) and a longpass filter (Thorlabs, FGL435M). The photoluminescence was then focused at the imaging plane at 495× magnification using a tube lens (Thorlabs, TTL200-S8) followed by a telescope (Thorlabs, AC254-030-A and AC254-125-A). An avalanche photo diode detector (APD, Micro Photon Devices, ~50 ps time resolution, 50 μm × 50 μm active area) was raster scanned over the two-dimensional image of the photoluminescence using two motors (Thorlabs ZFS25B). The PL decay curves collected at each point in the image were combined to reconstruct the temporal evolution of the exciton profile in the sample.

1.6. Steady-state spectroscopic characterization

Steady-state spectroscopic characterization of the SLs was performed using the same mounting conditions and excitation conditions as the TPLM measurements, except with the laser fluence increased to 0.12 μJ/cm^2. After passing through the tube lens, the fluorescence was redirected using a multimode fiber (Thorlabs, BFL105LS02) into a spectrograph (Princeton Instruments Acton SP2500), dispersed using a 300 groove/mm grating, and collected using an intensified CCD camera (Princeton Instruments, PI-MAX®4).

S2. Calculation of exciton diffusivity from microscopy measurements

2.1. Calculation of diffusivity values

The general diffusion equation in the low-excitation density regime can be written as:

$$\frac{\partial n(\boldsymbol{x},t)}{\partial t} = \nabla \cdot \left(\boldsymbol{D}\nabla n(\boldsymbol{x},t)\right) - kn(\boldsymbol{x},t) \tag{1}$$

where $n(\boldsymbol{x},t)$ is the exciton density distribution as a function of location $\boldsymbol{x}$ and time t, $\boldsymbol{D}$ is the exciton diffusivity tensor, and k is the linear decay rate constant. Here, we assume that the exciton diffusivity and decay rate are constant over the initial, rapid decay of the PL that we use to calculate diffusivities. If the initial exciton profile is given by $n(\boldsymbol{x},0)$, then the general solution to eqn. 1 in two dimensions is:

$$n(\boldsymbol{x},t) = e^{-kt}\frac{1}{4\pi t\sqrt{\det[\boldsymbol{D}]}}\int_{-\infty}^{\infty}\int_{-\infty}^{\infty} n(\tilde{\boldsymbol{x}},0)\exp\left[-\frac{1}{2}(\boldsymbol{x}-\tilde{\boldsymbol{x}})^{\mathsf{T}}(2\boldsymbol{D}t)^{-1}(\boldsymbol{x}-\tilde{\boldsymbol{x}})\right]d\tilde{\boldsymbol{x}} \tag{2}$$

where det represents the determinant, and the integral is taken over both dimensions of $\tilde{\boldsymbol{x}}$. After normalizing the PL profile at each time, we can write it as:

$$\begin{aligned} n(\boldsymbol{x},t) &\propto \int_{-\infty}^{\infty}\int_{-\infty}^{\infty} n(\tilde{\boldsymbol{x}},0)\exp\left[-\frac{1}{2}(\boldsymbol{x}-\tilde{\boldsymbol{x}})^{\mathsf{T}}(2\boldsymbol{D}t)^{-1}(\boldsymbol{x}-\tilde{\boldsymbol{x}})\right]d\tilde{\boldsymbol{x}} \\ &= n(\boldsymbol{x},0)\otimes \mathrm{N}(\boldsymbol{0},2\boldsymbol{D}t) \end{aligned} \tag{3}$$

Here, $\mathrm{N}(\mathbf{0}, \boldsymbol{\Sigma})$ denotes a two-dimensional Gaussian distribution with a mean of $\mathbf{0}$ and a 2×2 covariance matrix of $\boldsymbol{\Sigma} = 2\boldsymbol{D}t$, and the $\otimes$ symbol represents convolution. In this work, however, we fit diffusivity values based on one-dimensional slices of two-dimensional datasets. We extracted the one-dimensional data sets by sampling the full 2D data set at points along an oriented angle θ that passed through the peak of the PL profile. We kept the number of points and point spacing consistent at each θ, and we used linear interpolation to estimate the PL profile at points that did not exactly fall on a raster scan point. To determine the diffusivity along a line pointing at an angle of θ, we use the one-dimensional version of eqn. 3, replacing $\boldsymbol{D}$ with the scalar D_{eff} representing the effective diffusivity along that line.

$$n(x,t) \propto \int_{-\infty}^{\infty} n(\tilde{x},0) \exp\left[-\frac{x^2}{2\left(2D_{eff}t\right)}\right] d\tilde{x} = n(x,0) \otimes \mathrm{N}(0, 2D_{eff}t) \tag{4}$$

The initial profile $n(\tilde{x}, 0)$ in eqn. 4 is commonly assumed to be Gaussian. In this case, since the measured PL profiles were not well-fit by a Gaussian function, we instead use a modified version of the numerical convolution approach introduced by Hickey and Grumstrup.[8] In this method, each PL profile at times $t > 0$ is fit using a numerical convolution of a Gaussian function and the measured PL profile at $t = 0$:

$$n(x,t) \propto n(x,0) \otimes \mathrm{N}(0, \sigma(t)^2) \tag{5}$$

The diffusivities are then calculated based on the growth in the variance of the Gaussian function using the relationship $D_{eff} = \sigma(t)^2/(2t)$.

Although the numerical convolution approach does a better job of capturing the profile shape, it can struggle to accurately fit noisy data. As described, the numerical convolution approach is prone to overfitting, since it uses the noisy measurement of the initial profile to perform convolutions. Additionally, since $\sigma(t)^2$ cannot be negative, the numerical convolution approach

tends to overestimate the value of $\sigma(t)^2$, especially in cases when the initially measured profile $n(x,0)$ appears broader due to noise. This overestimation of variances has the greatest effect at early times, when the true value of $\sigma(t)^2 = 2D_{eff}t$ is closest to 0. As a result, the numerical convolution approach can result in systematic underestimation of the diffusivity values.

To address these issues, we modified the numerical convolution approach by convolving both sides of eqn. 5 with an additional Gaussian having a standard deviation of σ_b.

$$n(x,t) \otimes \mathrm{N}(0,\sigma_b^2) \propto n(x,0) \otimes \mathrm{N}(0,\sigma(t)^2) \otimes \mathrm{N}(0,\sigma_b^2) \quad (6)$$

This acts as a low-pass filter, removing the effects of noise at high spatial frequencies while mostly preserving the shape of the PL profile at low spatial frequencies. Additionally, since the convolution of two Gaussians is another Gaussian, we can write eqn. 6 as:

$$n(x,t) \otimes \mathrm{N}(0,\sigma_b^2) \propto n(x,0) \otimes \mathrm{N}(0,\sigma(t)^2 + \sigma_b^2) = n(x,0) \otimes \mathrm{N}\left(0,\sigma_f(t)^2\right) \quad (7)$$

After finding the value of $\sigma_f(t)^2 = \sigma(t)^2 + \sigma_b^2$ that fits the smoothed profile $n(x,t) \otimes \mathrm{N}(0,\sigma_b^2)$, we can subtract off the variance σ_b^2 added by the additional Gaussian convolution to recover the value of $\sigma(t)^2$. Since it is possible for the best fit of $\sigma_f(t)^2$ to be less than σ_b^2, this allows us to recover negative values of $\sigma(t)^2$, correcting for the overestimation seen without this additional convolution step. We used a value of $\sigma_b = 100$ nm in our analysis, which was large enough to prevent the overestimation of the Gaussian variances without significantly distorting the measured profiles. We used a linear fit to the initial values of $\sigma_f(t)^2$ to calculate the effective diffusivity at each angle using the relationship:

$$D_{eff} = \frac{\left(\sigma_f(t)^2 - \sigma_b^2\right)}{2t} \quad (8)$$

2.2. Effects of anisotropic exciton transport on microscopy data

In general, the growth in the variance of the PL profile as a function of angle can change in a complex, non-linear fashion. If we consider the changes in eqn. 3 along the line $\boldsymbol{r} = r[\cos(\theta)\ \sin(\theta)]^{\mathsf{T}}$, we obtain the following expression:

$$n(\boldsymbol{r},t) \propto \int_{-\infty}^{\infty}\int_{-\infty}^{\infty} n(\tilde{\boldsymbol{x}},0)\exp\left[-\frac{1}{2}\left(r\begin{bmatrix}\cos(\theta)\\ \sin(\theta)\end{bmatrix}-\tilde{\boldsymbol{x}}\right)^{\mathsf{T}}(2\boldsymbol{D}t)^{-1}\left(r\begin{bmatrix}\cos(\theta)\\ \sin(\theta)\end{bmatrix}-\tilde{\boldsymbol{x}}\right)\right]d\tilde{\boldsymbol{x}} \qquad (9)$$

If the initial profile is a Dirac delta function, then eqn. 9 becomes:

$$n(\boldsymbol{r},t) \propto \exp\left[-\frac{r^2}{2}\begin{bmatrix}\cos(\theta)\\ \sin(\theta)\end{bmatrix}^{\mathsf{T}}(2\boldsymbol{D}t)^{-1}\begin{bmatrix}\cos(\theta)\\ \sin(\theta)\end{bmatrix}\right] \qquad (10)$$

The diffusivity tensor is a symmetric matrix with two orthogonal eigenvectors and two eigenvalues that give the diffusivity in the direction of the corresponding eigenvectors. The contour lines of the Gaussian distribution in the above expression are ellipses whose major and minor axes are aligned with the eigenvectors of the diffusion tensor. Without loss of generality, we can use a coordinate system whose axes point along the eigenvectors of the diffusion tensor, which simplifies the diffusivity tensor to a diagonal matrix $D = \begin{bmatrix}D_1 & 0\\ 0 & D_2\end{bmatrix}$. We can then write eqn. 10 as:

$$n(\boldsymbol{r},t) \propto \exp\left[-\frac{r^2}{4t}\left(\frac{\cos^2\theta}{D_1}+\frac{\sin^2\theta}{D_2}\right)\right] \qquad (11)$$

Based on the variance of this Gaussian σ^2, the effective diffusivity at a given angle is then $D_{eff}(\theta) = \frac{\sigma^2}{2t} = \left(\frac{\cos^2\theta}{D_1}+\frac{\sin^2\theta}{D_2}\right)^{-1}$, which forms an ellipse in polar coordinates. However, the effective diffusivity can change based on the original profile shape. For example, if we take $n(\boldsymbol{x},0)$ to be an isotropic Gaussian with a covariance matrix of $\boldsymbol{\Sigma_0} = \begin{bmatrix}\sigma_0^2 & 0\\ 0 & \sigma_0^2\end{bmatrix}$, then using the fact that the convolution of two Gaussians is another Gaussian function, eqn. 9 becomes:

$$n(\boldsymbol{r}, t) \propto \exp\left[-\frac{r^2}{2}\left(\frac{\cos^2(\theta)}{\sigma_0^2 + 2D_1 t} + \frac{\sin^2(\theta)}{\sigma_0^2 + 2D_2 t}\right)\right] \tag{12}$$

The variance of this Gaussian varies nonlinearly with time, making the extraction of an effective diffusivity more challenging. However, if the expansion of the profile is small relative to its initial size, which is the case for our measurements on NC assemblies, then we can use the Taylor series expansion of the variance around $t = 0$ to extract a diffusivity term:

$$\begin{aligned}\sigma^2 = \left(\frac{\cos^2(\theta)}{\sigma_0^2 + 2D_1 t} + \frac{\sin^2(\theta)}{\sigma_0^2 + 2D_2 t}\right)^{-1} &\approx \sigma_0^2 + 2t(D_1 \cos^2(\theta) + D_2 \sin^2(\theta)) + O(t^2) \\ &= \sigma_0^2 + 2D_{eff} t + O(t^2)\end{aligned} \tag{13}$$

In the case of a small deviation from the original profile, the change in variance still grows linearly, and we can extract an effective diffusivity of $D_{eff}(\theta) = D_1 \cos^2(\theta) + D_2 \sin^2(\theta)$. This forms a sine wave as a function of θ, matching our measured effective diffusivities as a function of angle. Notably, although the functional form of $D_{eff}(\theta)$ changes depending on the initial profile shape, the underlying maximum and minimum diffusivities that we use to calculate diffusivity anisotropy ratios remain consistent.

S3. Calculation of theoretical diffusivity anisotropy ratios

3.1. Calculation of theoretical diffusivity anisotropy ratios from relative transport rates

We modeled energy transport in the A_2B-type superlattice using a three-dimensional $N \times N \times N$ array of $CsPbBr_3$ nanocrystals arranged in the A_2B structure based on the structural parameters in Table S1 and with periodic boundary conditions. The *c*-axis of the A_2B superlattice was aligned along the *z*-axis in our model. The energy transfer rates between each pair of dots were calculated based on the following equation for Förster resonance energy transfer (FRET):

$$k_{FRET} = \frac{k_{rad}}{d^6} \frac{9\kappa^2}{128\,\pi^5 n^4} J \tag{14}$$

Where k_{rad} is the radiative rate of the donor, d is the distance between the centers of the donor and the acceptor, κ^2 is the dipole orientation factor, n is the refractive index of the surrounding medium, and J is the spectral overlap integral. As described in the main text, we assumed that the k_{rad}, J, and κ^2 terms are constant for each pair of nanocrystals, so they do not contribute to the diffusivity anisotropy. Under this assumption, the energy transport rate can be expressed as:

$$k_{FRET} = C * \frac{1}{d^6 n^4} \tag{15}$$

where C is a constant. We set $C = 7.2 \times 10^7$ $\mathrm{nm^6 ns^{-1}}$ so that our calculated diffusivities would roughly match our experimental results; however, this choice is arbitrary and does not affect the final values for the diffusivity anisotropy.

We then used eqn. 15 to calculate the energy transfer rates between one arbitrarily chosen nanocrystal and every other nanocrystal in our model. By symmetry, the same energy transfer rates and distances apply for every nanocrystal in our model. For the case of an isotropic refractive index, we used $n = 1.79$ based on the volumetrically weighted average of the real dielectric constants of each component of the A_2B-type superlattice. For the case of an anisotropic refractive index, we used $n_z = n_{\parallel} = 1.79$ for the direction along the *c*-axis and $n_x = n_y = n_{\perp} = 1.70$ for directions in the *ab*-plane based on effective medium theory (see section 3.2). The effective refractive index between each pair of nanocrystals was calculated based on eqn. 16, where $\hat{\boldsymbol{d}}_{\boldsymbol{ij}}$ is a unit vector pointing in the direction from nanocrystal i to nanocrystal j.

$$n_{ij} = n_x \hat{d}_{ij,x} + n_y \hat{d}_{ij,y} + n_z \hat{d}_{ij,z} \tag{16}$$

We then used these transfer rates and hopping distances to calculate the expected change in the variance of the position of exciton along the axes of our superlattice $\hat{\boldsymbol{x}}$, $\hat{\boldsymbol{y}}$, and $\hat{\boldsymbol{z}}$. Then, we

calculated the diffusivity based on the change in variance in each direction (eqn. 17). The diffusivity of an exciton along the direction of any unit vector $\hat{\boldsymbol{v}}$ can be written as:

$$D_v = \frac{1}{2}\sum_{j\neq i} k_{ij}\left(\boldsymbol{d_{ij}}\cdot\hat{\boldsymbol{v}}\right)^2 \tag{17}$$

where the sum is taken over the energy transfer rates k_{ij} from one site i to every other site $j \neq i$, and $\boldsymbol{d_{ij}}$ is the displacement vector pointing from site i to j.

To find the diffusivity in the limit of an infinitely large lattice, we calculated the diffusivity in a series of progressively larger lattices from $N = 20$ to $N = 116$. As N increased, the diffusivity along each direction asymptotically approached its limiting value for an infinitely large lattice as $1/N$. We determined the limiting diffusivity D_∞ in each direction by fitting the diffusivity in each direction to the following functional form (see Figure S5):

$$D(N) = D_\infty - \frac{b}{N} \tag{18}$$

where b and c are additional fitting parameters. We then calculated the diffusivity anisotropy ratios by comparing the values of $D_{\infty,z}$ to $D_{\infty,x}$ and $D_{\infty,y}$.

3.2. Calculation of anisotropic refractive indices

To calculate the anisotropic refractive index in the A_2B-type superlattice, we used the effective medium approach for periodic arrays of tubular structures described by Reyes et al.[9] and Godin.[10] In our calculations, we used values of 7.3 and 2.58 for the real components of the relative permittivity of $CsPbBr_3$ and LaF_3, respectively.[11,12] We assumed the real component of the relative permittivity of the organic ligands was 2.25, a value representative of long hydrocarbon chains.[12] We approximated the A_2B superlattice as a regular hexagonal array of two-component cylindrical tubes, where the inside of each tube represents the combination of organic ligands and $CsPbBr_3$ cores at the center of each $CsPbBr_3$ nanocrystal column, the outer layer of each tube represents the

organic ligands, and the surrounding medium represents the LaF_3 nanodisks. The distance between tubes was set to 13 nm. We used a relative permittivity of $\epsilon = 6.4$ for the inside of each tube, calculated by taking the weighted average of the relative permittivities of the $CsPbBr_3$ core and the ligands along a line through the center of the $CsPbBr_3$ nanocrystal columns: We set the inner and outer radii of the tubes in our model to 3.0 nm and 5.0 nm, respectively, to match the relative cross-sectional area of each component in our tubular model with the A_2B-type superlattice. Following ref.[9], the dielectric constant in the direction parallel to the tubes is the volumetrically weighted average of the dielectric constant of each component, or $\epsilon_z = 3.20$. We calculated the dielectric constants in the plane perpendicular to the columns by applying the methods in ref.[10] to our tubular model, obtaining values of $\epsilon_x = \epsilon_y = 2.88$. We then calculated the refractive indices in each direction by taking the square root of the dielectric constants.

3.3. Application of the extended dipole approximation to energy transfer rates

To account for the effects of delocalization of the exciton in the $CsPbBr_3$ nanocrystals, we used an approach similar to that used by Kodaimati et al.[13] We treated the overall transition dipole moment of the exciton as a series of infinitesimal point dipoles extended throughout the cube, each with transition dipole strength proportional to the spatial probability distribution of the exciton at that point. Then, the overall coupling strength between the donor and the acceptor can be calculated by combining the transition dipole interactions of each pair of infinitesimal point dipoles in the donor and acceptor. We approximated the exciton wavefunction using the ground state particle-in-a cube state. For a cube centered at $\boldsymbol{r_0}$ and with side length l, this can be written as:

$$\psi(\boldsymbol{r}) = \begin{cases} \prod_{i=x,y,z} \sqrt{\frac{2}{l}} \cos\left(\frac{\pi}{l}(r_i - r_{0,i})\right), & -\frac{l}{2} \le r_x - r_{0,x} \le \frac{l}{2} \\ & -\frac{l}{2} \le r_y - r_{0,y} \le \frac{l}{2} \\ & -\frac{l}{2} \le r_z - r_{0,z} \le \frac{l}{2} \\ 0, & otherwise \end{cases} \quad (19)$$

Additionally, we assumed that the effective refractive indices were the same for each pair of point dipoles, and we assumed the orientation constant κ^2 in the FRET rate equation was $2/3$ for each pair of point dipoles, which is the orientationally averaged value for random, freely rotating dipoles. Under these assumptions, we can write the coupling strength for the extended dipoles (J_{ED}) relative to the coupling strength under the point dipole approximation (J_{PDA}, equivalent to the coupling strength used in conventional FRET theory) solely in terms of the distances between the different parts of the wavefunctions. For two nanocrystals whose centers are separated by a distance of d, the relative enhancement in coupling strength is:

$$\frac{J_{ED}}{J_{PDA}} = d^3 * \int \int \frac{|\psi_1(\boldsymbol{r_1})\psi_2(\boldsymbol{r_2})|^2}{|\boldsymbol{r_1} - \boldsymbol{r_2}|^3} d\boldsymbol{r_2}\, d\boldsymbol{r_1} \quad (20)$$

Since the exciton transfer rate is proportional to the coupling strength squared, the enhancement of the exciton transport rates k under the extended dipole approximation *versus* the point dipole approximation can be written as:

$$\frac{k_{ED}}{k_{PDA}} = \left(\frac{J_{ED}}{J_{PDA}}\right)^2 = d^6 * \left(\int \int \frac{|\psi_1(\boldsymbol{r_1})\psi_2(\boldsymbol{r_2})|^2}{|\boldsymbol{r_1} - \boldsymbol{r_2}|^3} d\boldsymbol{r_2}\, d\boldsymbol{r_1}\right)^2 \quad (21)$$

We used numerical integration to evaluate eqn. 21 for excitons in two axially aligned cubes with side lengths of 5.3 nm and with centers located at the origin and $[d \quad 0 \quad 0]^\mathsf{T}$ for different values of d (Figure S7). We then used these values to modify the FRET rates between each pair of nanocrystals in our model of the A_2B-type lattice based on the center-to-center distance between the nanocrystals. Finally, we used these enhanced energy transport rates to calculate the diffusivity

anisotropy ratios under the extended dipole approximation using the same methods described in section S3.1.

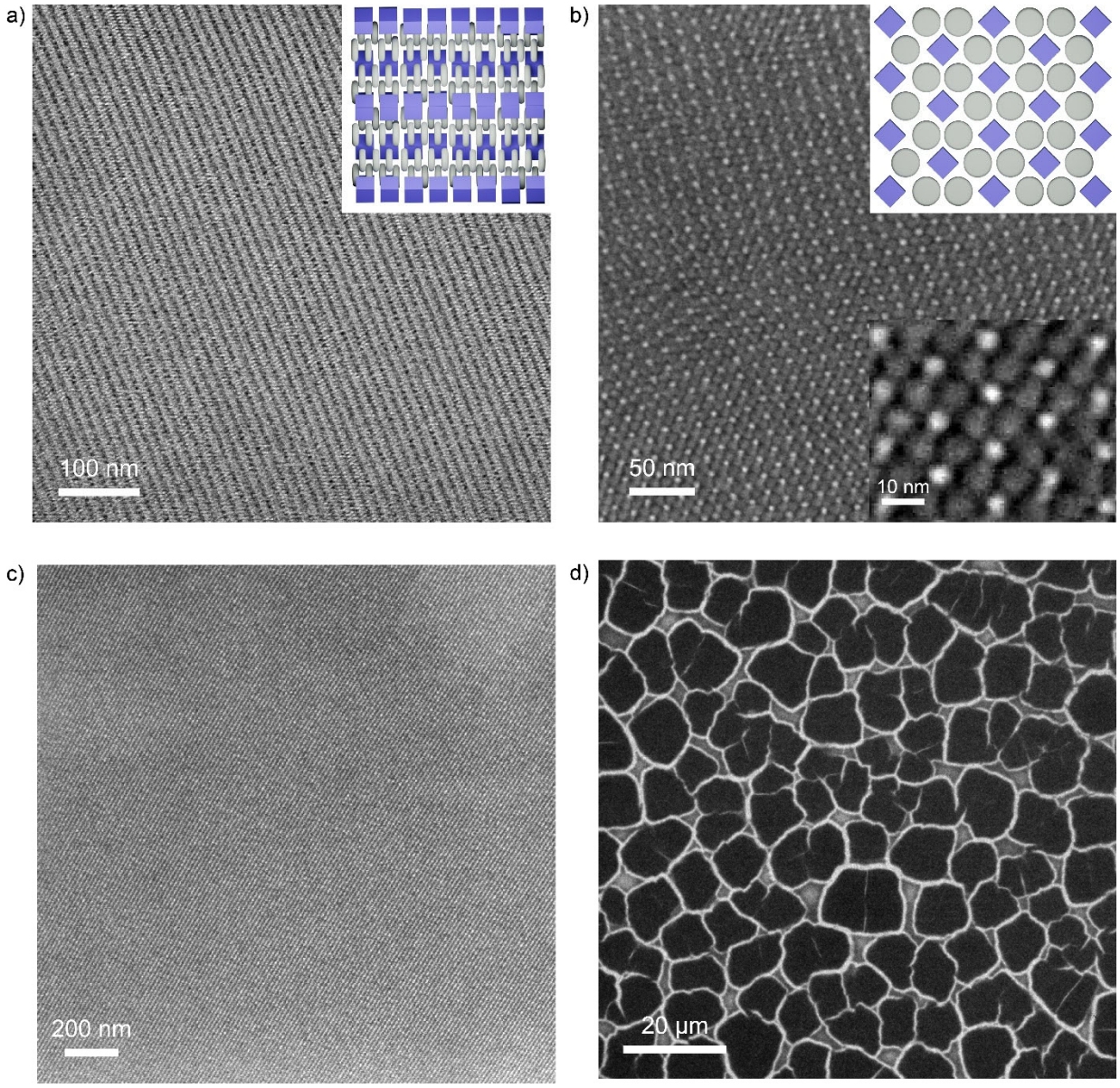

Figure S1. a) BF-STEM image of the A_2B-type superlattice, showing the NC assembly structure with columns lying flat on the surface. Structural model is contained in the inset. b) DF-STEM image of an A_2B-type superlattice domain at an alternate orientation, with the columns standing straight up on the surface. c) DF-STEM image of an A_2B-type superlattice domain, showing structural coherence over a wider area. d) Low-magnification TEM image of the A_2B-type superlattice, showing ~10 µm-sized superlattice domains.

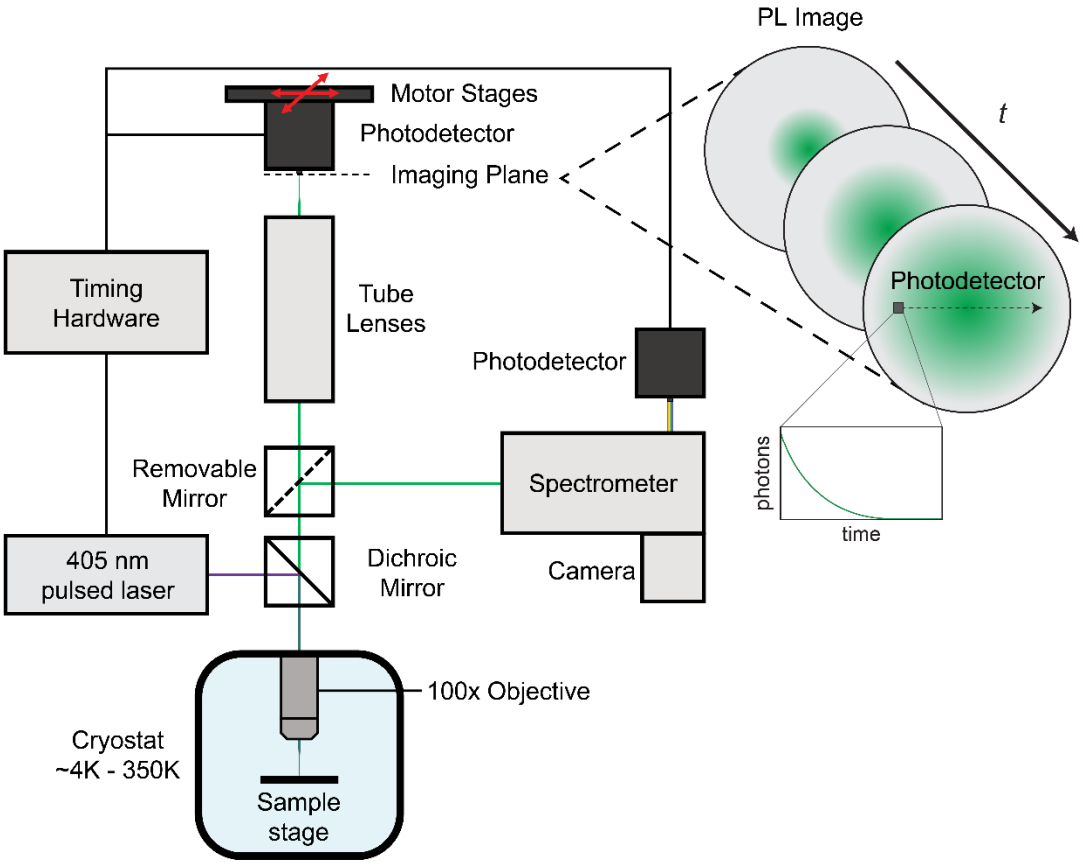

Figure S2. Diagram of our cryomicroscope setup used for exciton diffusion measurements and spectroscopic characterization.

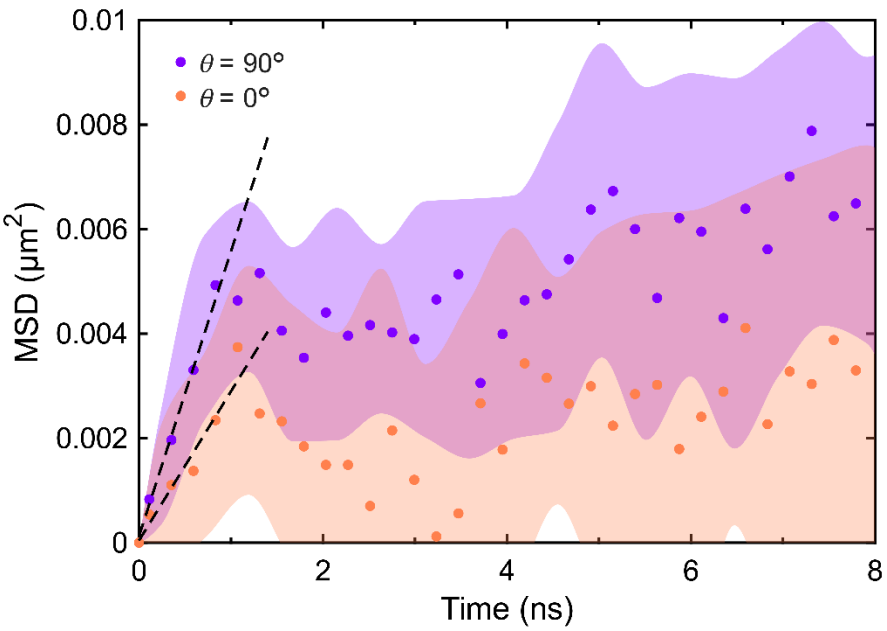

Figure S3. Mean squared displacement (MSD) of the exciton population in the A_2B-type superlattice at 5 K along two directions extracted from a two-dimensional scan. The MSDs are shown for $\theta = 90°$, approximately corresponding to the direction of the highest measured exciton diffusivity, and $\theta = 0°$, approximately corresponding to the direction of the lowest measured exciton diffusivity. The shaded regions indicate the standard deviation of the MSDs measured in each 480 ps interval.

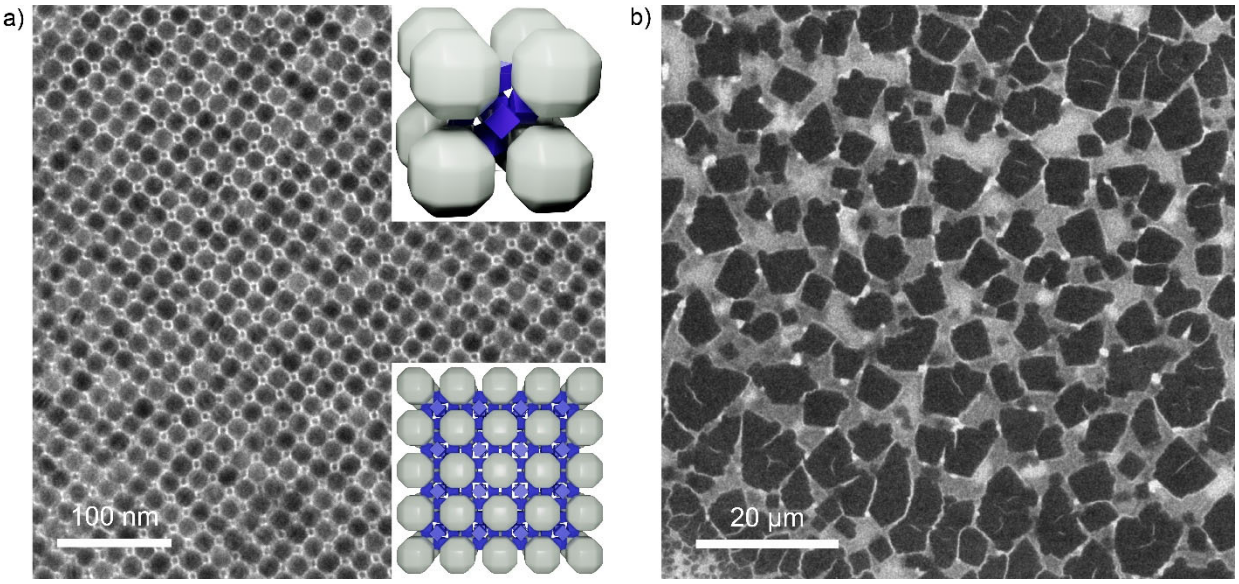

Figure. S4. a) TEM image of the ABO_6-type superlattice, showing the NC assembly structure, with structural models in the insets. b) Low-magnification TEM image of the ABO_6-type superlattice, showing individual superlattice domains.

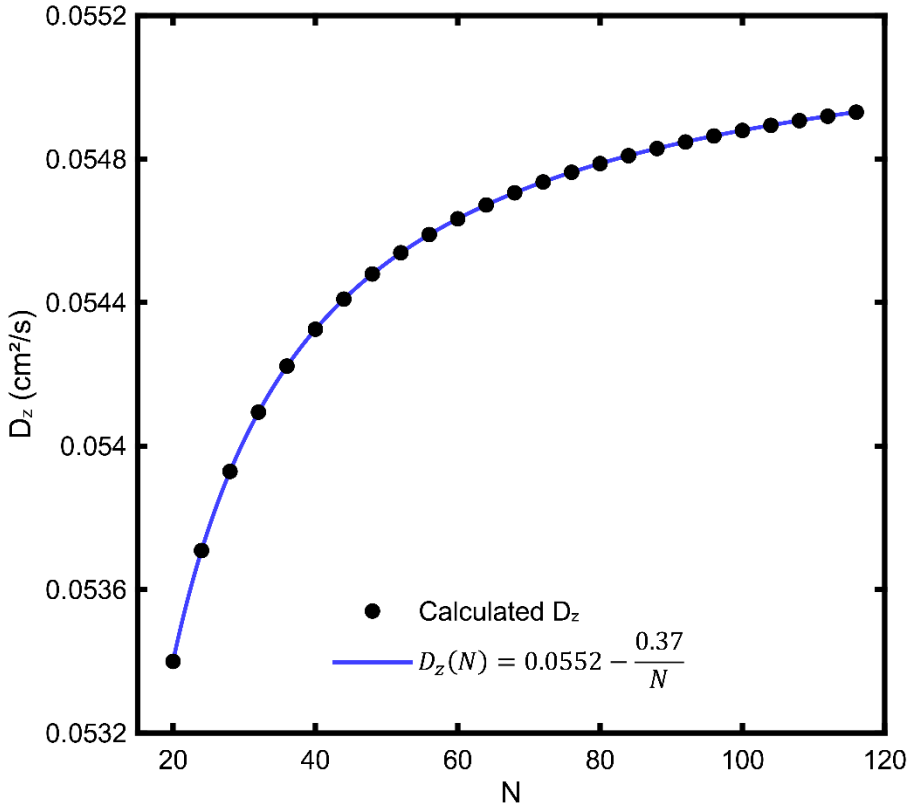

Figure S5. Example fit of calculated diffusivity data along the z-axis in model A_2B-type superlattices with isotropic refractive indices and using the point dipole approximation. As the system size N increases, the calculated diffusivity approaches the limiting value of $D_{\infty,z} = 0.0552 \frac{cm^2}{s}$, with the distance from this limit decreasing as $1/N$.

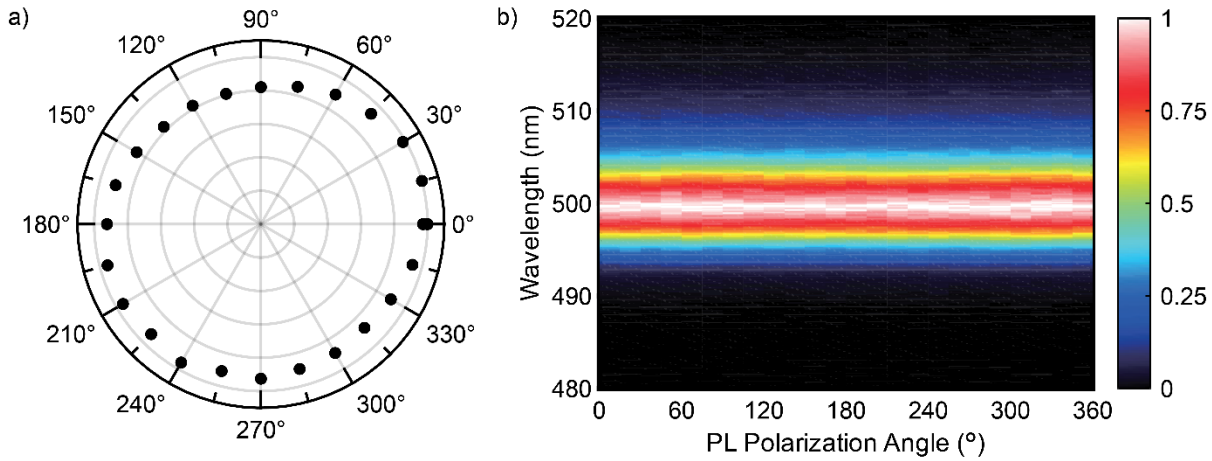

Figure S6. a) Linear polarization-resolved photoluminescence (PL) intensity from the A_2B superlattice at 5 K excited with circularly polarized light at 405 nm. b) Polarization-resolved normalized PL spectra from the A_2B superlattice at 5 K excited with circularly polarized laser light at 405 nm.

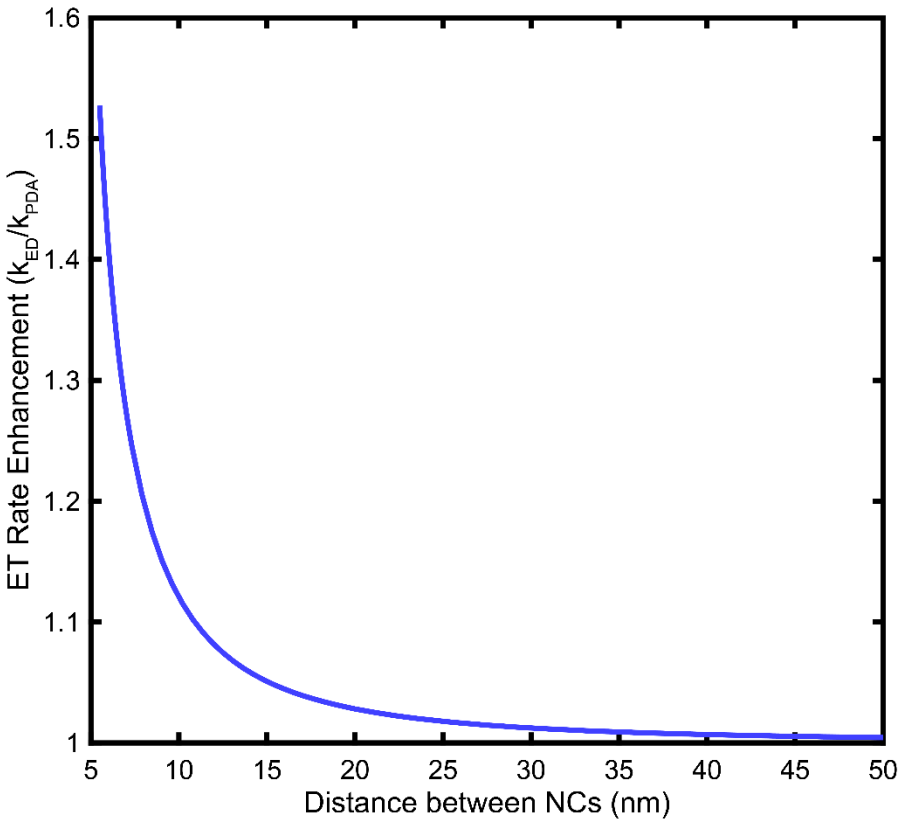

Figure S7. Predicted enhancement in exciton transfer (ET) rate as a function of center-center distance between nanocrystals (NCs) as a result of calculating the dipole coupling using the extended dipole approximation (k_{ED}) as described in section S3.3 *vs*. using the point dipole approximation (k_{PDA}).

Table S1. Structural parameters for the A_2B-type superlattice, obtained from Ref.[6]

$CsPbBr_3$ NC core side length	5.3 nm
$CsPbBr_3$ NC hard-cube edge length (also center-center intracolumnar separation)	6.42 nm
$CsPbBr_3$ NC intercolumnar separation	13 nm
LaF_3 nanodisk core diameter	6.5 nm

References:

(1) Sekh, T. V.; Cherniukh, I.; Kobiyama, E.; Sheehan, T. J.; Manoli, A.; Zhu, C.; Athanasiou, M.; Sergides, M.; Ortikova, O.; Rossell, M. D.; Bertolotti, F.; Guagliardi, A.; Masciocchi, N.; Erni, R.; Othonos, A.; Itskos, G.; Tisdale, W. A.; Stöferle, T.; Rainò, G.; Bodnarchuk, M. I.; Kovalenko, M. V. All-Perovskite Multicomponent Nanocrystal Superlattices. *ACS Nano* **2024**, *18* (11), 8423–8436. https://doi.org/10.1021/acsnano.3c13062.

(2) Protesescu, L.; Yakunin, S.; Bodnarchuk, M. I.; Krieg, F.; Caputo, R.; Hendon, C. H.; Yang, R. X.; Walsh, A.; Kovalenko, M. V. Nanocrystals of Cesium Lead Halide Perovskites (CsPbX(3), X = Cl, Br, and I): Novel Optoelectronic Materials Showing Bright Emission with Wide Color Gamut. *Nano Lett* **2015**, *15* (6), 3692–3696. https://doi.org/10.1021/nl5048779.

(3) Dong, Y.; Qiao, T.; Kim, D.; Parobek, D.; Rossi, D.; Son, D. H. Precise Control of Quantum Confinement in Cesium Lead Halide Perovskite Quantum Dots via Thermodynamic Equilibrium. *Nano Lett.* **2018**, *18* (6), 3716–3722. https://doi.org/10.1021/acs.nanolett.8b00861.

(4) Boehme, S. C.; Bodnarchuk, M. I.; Burian, M.; Bertolotti, F.; Cherniukh, I.; Bernasconi, C.; Zhu, C.; Erni, R.; Amenitsch, H.; Naumenko, D.; Andrusiv, H.; Semkiv, N.; John, R. A.; Baldwin, A.; Galkowski, K.; Masciocchi, N.; Stranks, S. D.; Rainò, G.; Guagliardi, A.; Kovalenko, M. V. Strongly Confined CsPbBr3 Quantum Dots as Quantum Emitters and Building Blocks for Rhombic Superlattices. *ACS Nano* **2023**, *17* (3), 2089–2100. https://doi.org/10.1021/acsnano.2c07677.

(5) Bera, S.; Behera, R. K.; Pradhan, N. α-Halo Ketone for Polyhedral Perovskite Nanocrystals: Evolutions, Shape Conversions, Ligand Chemistry, and Self-Assembly. *J. Am. Chem. Soc.* **2020**, *142* (49), 20865–20874. https://doi.org/10.1021/jacs.0c10688.

(6) Cherniukh, I.; Rainò, G.; Sekh, T. V.; Zhu, C.; Shynkarenko, Y.; John, R. A.; Kobiyama, E.; Mahrt, R. F.; Stöferle, T.; Erni, R.; Kovalenko, M. V.; Bodnarchuk, M. I. Shape-Directed Co-Assembly of Lead Halide Perovskite Nanocubes with Dielectric Nanodisks into Binary Nanocrystal Superlattices. *ACS Nano* **2021**, *15* (10), 16488–16500. https://doi.org/10.1021/acsnano.1c06047.

(7) Paik, T.; Diroll, B. T.; Kagan, C. R.; Murray, C. B. Binary and Ternary Superlattices Self-Assembled from Colloidal Nanodisks and Nanorods. *J. Am. Chem. Soc.* **2015**, *137* (20), 6662–6669. https://doi.org/10.1021/jacs.5b03234.

(8) Hickey, C. L.; Grumstrup, E. M. Reduced Artifact Approach for Determining Diffusion Coefficients in Time-Resolved Microscopy. *J. Phys. Chem. C* **2020**, *124* (25), 14016–14021. https://doi.org/10.1021/acs.jpcc.0c02302.

(9) Reyes, E.; Krokhin, A. A.; Roberts, J. Effective Dielectric Constants of Photonic Crystal of Aligned Anisotropic Cylinders and the Optical Response of a Periodic Array of Carbon Nanotubes. *Phys. Rev. B* **2005**, *72* (15), 155118. https://doi.org/10.1103/PhysRevB.72.155118.

(10) Godin, Y. A. Effective Properties of Periodic Tubular Structures. *The Quarterly Journal of Mechanics and Applied Mathematics* **2016**, *69* (2), 181–193. https://doi.org/10.1093/qjmam/hbw003.

(11) Yang, Z.; Surrente, A.; Galkowski, K.; Miyata, A.; Portugall, O.; Sutton, R. J.; Haghighirad, A. A.; Snaith, H. J.; Maude, D. K.; Plochocka, P.; Nicholas, R. J. Impact of the Halide Cage

on the Electronic Properties of Fully Inorganic Cesium Lead Halide Perovskites. *ACS Energy Lett.* **2017**, *2* (7), 1621–1627. https://doi.org/10.1021/acsenergylett.7b00416.
(12) Polyanskiy, M. N. Refractiveindex.Info Database of Optical Constants. *Sci Data* **2024**, *11* (1), 94. https://doi.org/10.1038/s41597-023-02898-2.
(13) Kodaimati, M. S.; Wang, C.; Chapman, C.; Schatz, G. C.; Weiss, E. A. Distance-Dependence of Interparticle Energy Transfer in the Near-Infrared within Electrostatic Assemblies of PbS Quantum Dots. *ACS Nano* **2017**, *11* (5), 5041–5050. https://doi.org/10.1021/acsnano.7b01778.